Geochemistry
Geophysics
Geosystems
G³

Published by AGU and the Geochemical Society

Article
Volume 14, Number 3
19 March 2013
doi:10.1029/2012GC004241
ISSN: 1525-2027

Temperature dependence of frictional healing of Westerly granite: Experimental observations and numerical simulations

E. K. Mitchell, Y. Fialko, and K. M. Brown
Institute of Geophysics and Planetary Physics, Scripps Institution of Oceanography, University of California, San Diego, La Jolla, California, USA

[1] Temperature is believed to have an important control on frictional properties of rocks, yet the amount of experimental observations of time-dependent rock friction at high temperatures is rather limited. In this study, we investigated frictional healing of Westerly granite in a series of slide-hold-slide experiments using a direct shear apparatus at ambient temperatures between 20°C and 550°C. We observed that at room temperature coefficient of friction increases in proportion to the logarithm of hold time at a rate consistent with findings of previous studies. For a given hold time, the coefficient of friction linearly increases with temperature, but temperature has little effect on the rate of change in static friction with hold time. We used a numerical model to investigate whether time-dependent increases in real contact area between rough surfaces could account for the observed frictional healing. The model incorporates fractal geometry and temperature-dependent viscoelasoplastic rheology. We explored several candidate rheologies that have been proposed for steady state creep of rocks at high stresses and temperatures. None of the tested laws could provide an agreement between the observed and modeled healing behavior given material properties reported in the bulk creep experiments. An acceptable fit to the experimental data could be achieved with modified parameters. In particular, for the power-law rheology to provide a reasonable fit to the data, the stress exponent needs to be greater than 40. Alternative mechanisms include time-dependent gouge compaction and increases in bond strength between contacting asperities.

Components: 10,664 words, 10 figures.

Keywords: friction; asperity; rate and state; creep law; temperature; Westerly granite.

Index Terms: 8163 Tectonophysics: Rheology and friction of fault zones (8034); 8118 Tectonophysics: Dynamics and mechanics of faulting (8004); 5120 Physical Properties of Rocks: Plasticity, diffusion, and creep.

Received 17 May 2012; **Revised** 9 November 2012; **Accepted** 12 November 2012; **Published** 19 March 2013.

Mitchell, E. K., Y. Fialko, and K. M. Brown (2012), Temperature dependence of frictional healing of Westerly granite: experimental observations and numerical simulations, *Geochem. Geophys. Geosyst.*, *14*, 567–582, doi:10.1029/2012GC004241.

1. Introduction

[2] An important part of the seismic cycle is the increase in fault strength after the occurrence of rapid slip, also known as fault healing. Frictional healing has been documented in laboratory experiments on many rock types. Static coefficient of friction increases with the duration of time of stationary contact between rock surfaces under normal load [*Dieterich*, 1972]. The pioneering experimental

studies of frictional healing in rocks [*Dieterich*, 1972] were performed with a double direct shear apparatus at room temperature. The key observation was that static friction coefficient increases with the logarithm of time that surfaces are left in stationary contact. This is a reproducible phenomenon that is observed in many rock types and other materials such as metals, paper, glass, and acrylic for a wide range of experimental conditions [*Dieterich*, 1972; *Dieterich and Kilgore*, 1994; *Baumberger and Caroli*, 2006]. Subsequent studies have investigated the effects of humidity [*Dieterich and Conrad*, 1984; *Frye and Marone*, 2002], rock type, normal stress [*Dieterich*, 1972], shear stress [*Karner and Marone*, 2001], and loading rate [*Kato et al.*, 1992] on frictional healing. The effect of temperature was also explored [*Stesky et al.*, 1974; *Blanpied*, 1995; *Karner et al.*, 1997; *Nakatani*, 2001], but with the exception of *Nakatani* [2001], experimental constraints on the temperature dependence of frictional healing are rather limited. Recent findings from high-speed frictional experiments suggest that dramatic variations in the coefficient of friction at slip rates greater than 0.1 m/s may be thermally activated [*Tsutsumi and Shimamoto*, 1997; *Di Toro et al.*, 2011; *Brown and Fialko*, 2012]. Because coseismic heating effects can be significant [e.g., *Fialko*, 2004], one of the motivations of this study is to better understand the effects of pure temperature versus coupled temperature-slip rate dependence of frictional strength. Also, the importance of temperature control on the transition between velocity-weakening and velocity-strengthening behavior and, ultimately, the depth extent of the seismogenic layer [*Scholz*, 2002] warrants more experimental studies. Finally, quantifying the effect of temperature on fault healing will improve our understanding of the behavior of active faults at seismogenic depths.

[3] In this study, we focus on time-dependent evolution of true contact area as a possible mechanism of frictional healing. *Dieterich and Kilgore* [1994] reported that for analog materials (glass and acrylic), contact area increases with the logarithm of hold time and agrees well with the observed evolution of static friction. They argued that similar time dependence is evidence for the control of true contact area on frictional aging. If so, a similar mechanism may be applicable to a wide range of materials such as rock, metal, paper, glass, and acrylic, which all exhibit logarithmic strengthening with time [*Baumberger and Caroli*, 2006].

[4] A similar interpretation is provided by nanoindentation studies [*Goldsby et al.*, 2004]. *Goldsby et al.* [2004] compared fractional contact area calculated from indentation creep data on quartz with fractional contact area inferred from slide-hold-slide static friction tests on quartz. They found that contact area increase from the indentation tests was logarithmic in time and only 1.7 times larger than that inferred from static friction experiments. They suggested that the discrepancy was due to shear relaxation during the reloading portion of the slide-hold-slide tests. They argued that inelastic flow at asperities, which increases real contact area, is the most likely mechanism causing frictional healing.

[5] Here we report results from a series of slide-hold-slide laboratory experiments aimed to study the effects of elevated temperature on fault healing rates. We also evaluate the extent to which frictional healing can be described by increases in real contact area due to creep of asperities using a finite element model with fractal contact geometry.

2. Experimental Setup

[6] We conducted experiments using a heated direct shear apparatus (Figures 1a and 1b). Rectangular rock samples are pressed against each other within steel sample holders of matching geometry. The bottom sample holder is held stationary. The top sample is shorter than the bottom sample, so that it can slide over a distance of 40 mm while maintaining constant contact area. The top sample holder is pulled in the shear direction using a stepper motor. The stepper motor is controlled with a computer program (Shear Large), in which a series of velocity steps can be specified. The normal load is applied to the sample by a hydraulic pump which presses a ram onto the top sample. The hydraulic piston is attached to a track above the sample and can slide in the shear direction freely while it exerts a normal load. The normal load is held constant using a proportional-integral-derivative (PID) controller that is part of the data acquisition system. Electrical strip heaters are attached to both the top and bottom sample holders. We measure temperature using a thermistor that is inserted through a hole in the top sample holder so that it touches the sample. We built a furnace around the sample holders using insulating materials to hold temperature constant. Normal stress is measured using a load cell in compression that is directly connected to the top sample holder. It is calibrated using a pressure sensor on the hydraulic pump. The hydraulic pump is accurate to within about 0.15 MPa. The

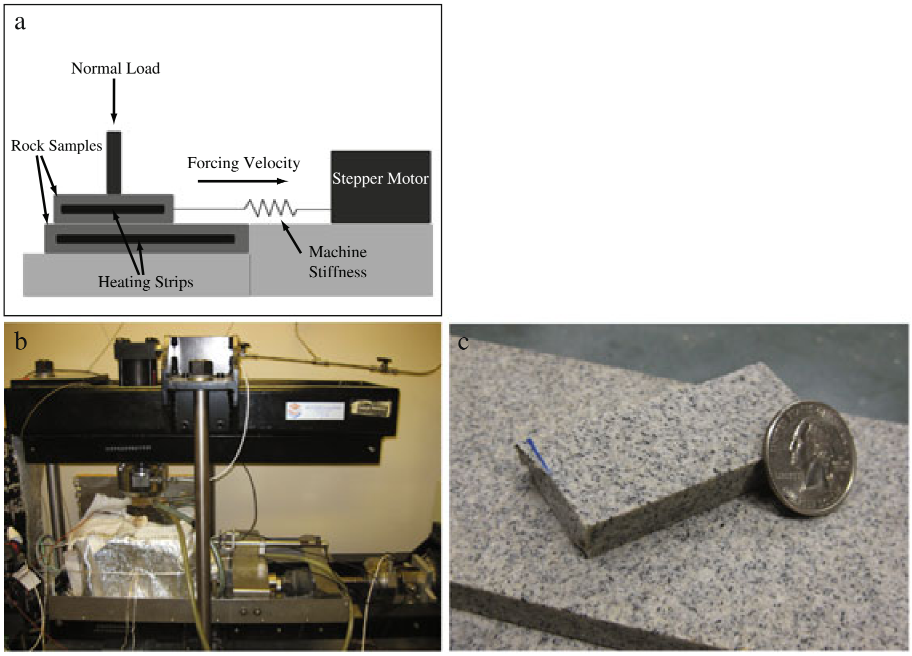

Figure 1. (a) Diagram of direct shear apparatus. (b) Photo of experimental setup. (c) Photo of Westerly granite.

shear stress is measured using a load cell in tension that is connected between the stepper motor and the bar that pulls the top sample. It is calibrated to the normal load cell, assuming a sliding coefficient of friction for Westerly granite of about 0.75. Both load cell calibrations are linear with an R^2 of about 0.995 over the range of 0.5–20 MPa. The shear displacement is measured using a linear voltage displacement transducer (LVDT) that is connected directly to the top and bottom sample holders. The LVDT is calibrated using the speed of the stepper motor. The LVDT is accurate to within about 1 μm and is linear with an R^2 of about 0.999 over the range of 10 mm. The data are collected from the transducers and digitized using Instrunet (http://www.instrunet.com/). Variations in friction due to heterogeneity within the sample shear zone are much larger ($\mu_o = 0.77 \pm 0.04$) than variations due to nonlinearity and analog-to-digital conversions. When the sample is sheared, a layer of gouge builds up between the rock surfaces. There is no sleeve to confine the wear particles between the samples, but very little gouge (about 5% of the total gouge by volume) is extruded out of the samples during testing and re-setting the samples.

[7] The apparatus can operate at driving velocity from less than 10^{-5} mm/s up to 0.1 mm/s. The machine's stiffness is 8.28 MPa/mm. We measured coefficient of friction in the temperature range from room temperature to 550°C. All the experiments reported here were conducted at constant normal stress of 15 MPa, driving speed of 0.01 mm/s, and room humidity. The nominal area of contact between samples is 2.64×10^3 square millimeters. The samples have been ground to a flatness of 4 μm/m and roughness of grit #80. We performed experiments on several rock types. Results presented here are for Westerly granite, which has been extensively used in previous studies. Westerly granite was chosen because it has been previously well characterized, and it is instructive to compare friction results at similar laboratory conditions [*Lockner et al.*, 1986; *Blanpied*, 1995; *Carter et al.*, 1981; *Tullis and Yund*, 1977; *Stesky*, 1978; *Beeler et al.*, 1996]. Westerly granite consists of about 30% quartz, 30% oligoclase, 30% microcline, and about 5–10% bioite, with an average grain size of about 0.75 mm (Figure 1c) [*Tullis and Yund*, 1977].

[8] The direct shear setup has several advantages over other types of experimental apparatuses. It can perform under a wide range of driving velocities and significant slip distances (up to hundreds of millimeters) compared to the widely used triaxial apparatus, which can only produce small displacements because of the geometry of the confining jacket around the sample [*Hoskins et al.*, 1968]. Large slip distances are beneficial because of significant evolution of friction coefficient within the first few tens of millimeters of slip, likely due to the buildup of gouge (wear particles) [e.g., *Beeler et al.*, 1996]. A typical run-in displacement in our experiments was about 80 mm, and the total cumulative displacement in our experiments was about 440 mm.

This is comparable to a "run-in" displacement of a few tens of millimeters and total displacement of greater than 400 mm reported by *Beeler et al.* [1996]. In a study by *Power et al*. [1988], gouge production was measured as a function of slip for solid Westerly granite samples. Their results showed an initial increase in wear particles with displacement, but eventually gouge production nearly stopped, and shear deformation was accommodated by the developed layer of granular material. This implies that results should not depend on total slip after the initial "run-in" displacement. Gouge fabric plays an important role in the frictional strength of faults [*Collettini et al*., 2009]. In our experimental setup, initially bare rock surfaces are sheared, and a gouge layer accumulates "naturally." This may be a better approximation of in situ fault conditions than either bare or "simulated" (ground and sieved) gouge, since the gouge has undergone some amount of shearing and has developed some fabric.

3. Procedure

[9] Initially, the sample was run-in (slid under normal stress) until friction reached a constant value. We employed a slide-hold-slide routine [*Dieterich*, 1972; *Beeler et al*., 1994; *Marone*, 1998a]. We placed the top sample at the edge of the bottom sample to allow the largest amount of slip in each run. Upon applying the normal stress of 15 MPa, we heated the sample to the desired ambient temperature. During the first part of a hold test, we applied the driving velocity until the sample either stably slid at constant shear stress or stick-slipped with nearly constant stress drop and recurrence interval. Then we sharply reduced the driving velocity (in case of stick-slip, right after a slip event). We held the sample under constant normal stress for the desired period of time. Then we resumed pulling at the imposed driving velocity and measured the peak value of shear stress right before the next slip event. We calculated friction coefficient by dividing the measured shear stress by normal stress (Figure 2a). We recorded the value of coefficient of friction right before the hold period, the peak value of friction right before rapid slip (μ_s) (Figure 2b), the minimum value of friction right after rapid slip ($\mu_{\min}$), as well as the time during quasi-stationary contact (hold time, t_h). See Figure (S1) of the Supplementary Materials for a description of these different measures of friction. The steps of slide, hold and slide were repeated to cover several orders of magnitude of hold time. Then we changed the ambient temperature and repeated the steps of slide-hold-slide until the slip distance equaled the difference in length between the top and bottom samples (40 mm). Subsequently, we reduced the normal stress to 0.5 MPa and moved the top sample back to the original position. We repeated tests in various sequences to ensure reproducible behavior. We conducted most tests for hold times between 7 s and 2×10^5 s (a few days), and one test was held for over a month (3.6×10^6 s). We applied temperature increments in both increasing and decreasing order to investigate possible temperature hysteresis effects. Eight runs in total were completed, and we kept track of the order in which the tests were conducted to monitor any dependence of friction on total slip. Figures (S2)–(S10) of the Supplementary Materials illustrate the respective results.

4. Experimental Results

[10] All tests revealed a logarithmic increase in static friction with hold time. On similar machines with granite samples at room temperature and about 15 MPa normal stress, we calculate healing rates similar to those reported by *Dieterich* [1972]: a few percent increase in static friction per decade hold time. For example, at room temperature, static coefficient of friction increases from 0.77 to 0.81 in 10^3 s (or 17 min). We fit our experimental data using an empirical expression proposed by *Dieterich* [1972]:

$$\mu_s = \mu_o + \beta \log_{10}(t_h) \quad (1)$$

where μ_s is static friction coefficient, μ_o is the value of static friction coefficient at 1 s (also referred to as "intercept" in this study), β is the logarithmic rate of increase in static friction coefficient (also referred to as "slope" in this study), and t_h is hold time. Equation (1) breaks down for hold times less than a few seconds [Nakatani and Scholz, 2006], but in our experiments the shortest hold times were about 7 s. Figure 3 shows all the μ_s data plus logarithmic fits using Equation (1). The increase in static friction coefficient with hold time represents an increase in the shear strength of the samples. The logarithmic rate of increase in shear strength with time can be calculated by multiplying the normal stress by the coefficient of friction and by the percent increase in coefficient of friction per decade (15 MPa × 0.7 × 0.025 decade^{-1} = 0.3 MPa/decade). Extrapolation of these results to conditions at seismogenic depths (effective normal stress of 100–200 MPa) gives rise to strengthening rates of a few megapascals per decade.

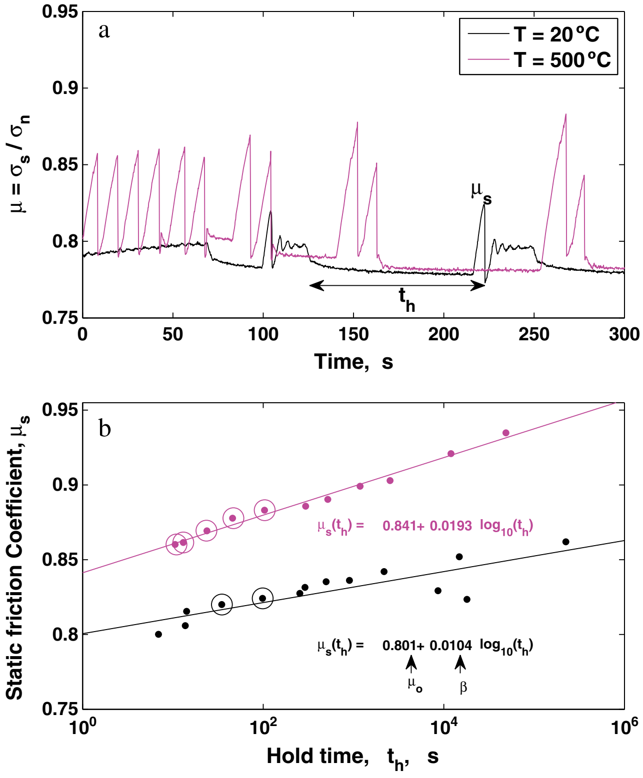

Figure 2. (a) Friction coefficient versus time. The black line represents hold tests conducted at room temperature, the magenta line represents tests conducted at 500°C. The arrow labeled t_h marks the beginning and end of a hold during which driving velocity decreased to zero for the room temperature test. The μ_s label indicates the maximum value of friction reached before slip for that hold time (static coefficient of friction). Note that alternating periods of "slide" and "hold" do not line up in time between the two different temperature runs. (b) Static coefficient of friction versus hold time. The circled dots represent values picked from data shown in Figure 2a.

[11] The experimental results show that static friction increases linearly with increasing temperature at about 0.02 per 140°C. For example, at room temperature, μ_o is 0.77, and at 500°C it is 0.83 (Figure 4a), which is an increase in coefficient of friction of 0.06. In the study of *Nakatani* [2001], hold tests were performed on feldspar powder using a double direct shear apparatus at similar pressure and temperature conditions to our experiments (Figure (S11a) of the Supplementary Materials). μ_o can be calculated from the data he presented in Table 1. Based on the data of *Nakatani* [2001], μ_o increases from 0.62 at room temperature to 0.69 at 600°C, which is an increase of 0.07 (Figure (S11b) of the Supplementary Materials). While our values for μ_o seem to be slightly higher, the temperature dependence of μ_o is in agreement with Nakatani's results.

[12] In the study of *Chester* [1995], the temperature dependence of steady state friction of dry granite gouge (from *Lockner et al.* [1986]) was compared to that of wet granite gouge (from *Blanpied et al.* [1991]). The coefficient of friction for dry granite gouge increased with temperature from about 0.70 at room temperature to about 0.75 at 500°C and continued to increase up to 900°C. The wet granite gouge data followed the dry data up to about 300°C, after which the coefficient of friction dropped dramatically between 300°C and 600°C to about 0.58. The temperature dependence of μ_o that we report is in agreement with the temperature dependence of sliding friction of dry granite gouge reported by *Lockner et al.* [1986]. Caution must be used in extrapolating laboratory results to natural faults, especially considering the uncertainty in pore fluid pressure and fluid saturation at depth. Assuming dry conditions, the neglect of temperature dependence gives rise to underestimation of the static fault strength by nearly 10%, (see Figures 3 and 4). However, the effect of temperature on fault strength may be offset in the presence of water [*Blanpied et al.*, 1991].

[13] Our results suggest that temperature does not significantly change the rate at which static friction increases with time. This relationship holds all the way up to the maximum tested temperature of

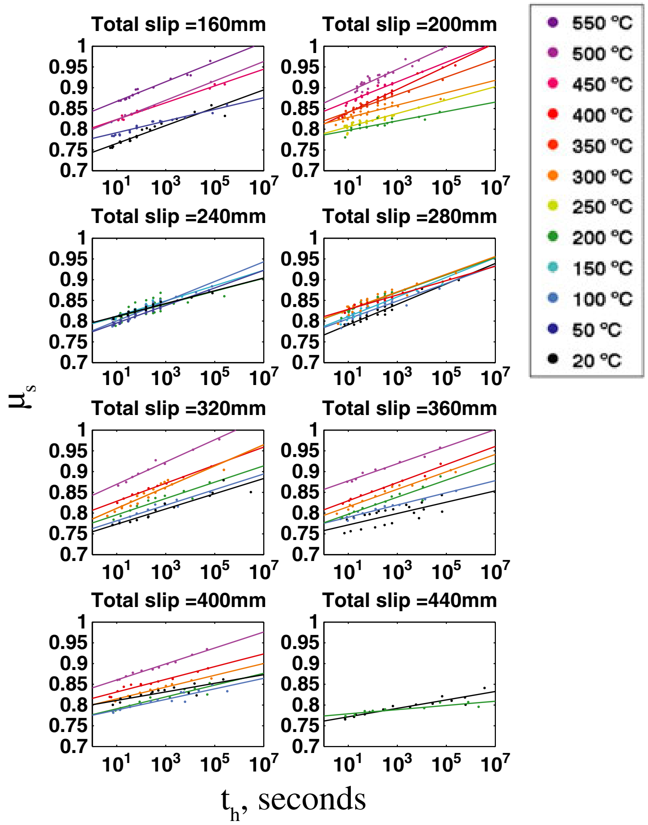

Figure 3. Static coefficient of friction μ_s versus hold time t_h. Measurements are shown with dots, least squares fits are shown with lines. Color represents temperature. Each plot consists of tests done in sequence without re-setting the sample. The titles display the total slip accumulated at the end of each plot.

550°C (Figure 4b). Figure 4 shows μ_o and β as a function of temperature for all of the data presented in Figure 3. At room temperature, we calculate β to be about 0.016, and at 500°C, we calculate β to be about 0.021. For comparison, β can also be calculated from the data of *Nakatani* [2001] (his Table 1). Based on his data, β increases from about 0.007 at room temperature to 0.0293 at 600°C. At room temperature, our value for β is higher than the values reported by Nakatani, but our results agree at higher temperature. Overall, Nakatani reports a stronger increase in β with temperature (Figure (S11c) of the Supplementary Materials).

[14] Our experimental results may be analyzed in the context of the rate-state friction laws [*Dieterich*, 1979; *Ruina*, 1983]:

$$\mu = \mu_* + a\ln\frac{V}{V_*} + b\ln\frac{V_*\theta}{D_c} \quad (2)$$

$$\frac{d\theta}{dt} = 1 - \frac{V\theta}{D_c} \quad (3)$$

where μ is the coefficient of friction, μ_* is the coefficient of friction at a reference velocity V_*, V is velocity, a is a constitutive parameter corresponding to the direct effect, b is a constitutive parameter corresponding to the evolution effect, θ is a state variable, and D_c is the critical displacement. If the conventional rate-state constitutive equations (Equations 2 and 3) are applied to a simple spring-slider model of friction, the parameter b can be calculated directly from our experiments, assuming that the state variable evolves according to an aging law (Equation 3) and not a slip law [*Beeler et al.*, 1994].

[15] At long hold times, b can be approximated by the following equation:

$$b = \frac{\Delta\mu_s}{\Delta\ln t_h} \quad (4)$$

[16] We calculate b as the slope of the curves in Figure 3 with logarithmic (base e) time. We estimate that b increases from 0.0092 at room temperature to 0.0118 at 500°C. We also fit the rate-state equations to time series of slip and μ from two of our hold tests (Figure S12 in the Supplementary

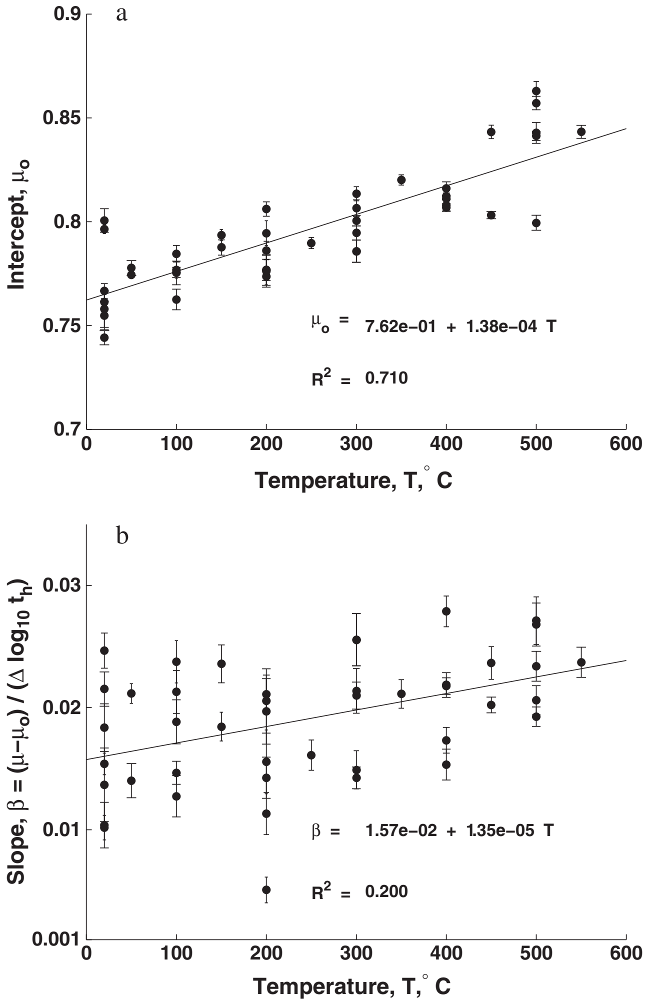

Figure 4. (a) Static coefficient of friction extrapolated to 1 s hold time, μ_o versus temperature, T. There is a linear relationship of about 0.02 per 140°C. (b) Rate of increase in static friction β versus temperature T. β is only weakly dependent on T.

Materials). We found that the data can be fit well at 20°C and 500°C using the values for b calculated using Equation (4) at those respective temperatures. In the study of *Blanpied et al.* [1998], the rate-state parameters a and b were fit to data from dry and wet granite velocity-stepping tests. *Blanpied et al.*, 1998 performed inversions for a and b on dry granite data from *Lockner et al.* [1986] and wet granite data from *Blanpied et al.*, [1991] and *Blanpied* [1995]. *Blanpied et al.* [1998] reported that for the dry granite data, b increased from 0.001 to 0.018 from 23°C to 845°C. The wet tests up to 350°C could be fit by similar values. The wet tests above 350°C, however, had to be fit using a second state variable, b_2, which decreases from -0.03 to -0.14 from 350°C to 600°C. In the low temperature range, the values for b that we report are higher than the values reported by *Blanpied et al.* [1998] for dry granite. In the high temperature range, the values for b that we report are close to the values reported by *Blanpied et al.* [1998] for dry granite. The following are three possible reasons for the discrepancy between our results and those of *Blanpied et al.* [1998]. The first is that experiments were performed on different kinds of samples (*Lockner et al.* [1986], *Blanpied et al.* [1991], and *Blanpied* [1995] used ground simulated granite gouge). The second is that the experiments were performed using different machine geometries (*Lockner et al.* [1986], *Blanpied et al.* [1991], and *Blanpied* [1995] used a triaxial setup, which only allows for small cumulative slip). The third is that the experimental procedures were different (*Lockner et al.* [1986], *Blanpied et al.* [1991], and *Blanpied* [1995] performed velocity-stepping tests under stable sliding conditions).

[17] Another result of the inversions of *Blanpied et al*. [1998] was the value of $(a - b)$ as a function of temperature. For dry granite, $(a - b)$ was close to zero at all temperatures. For wet granite, $(a - b_1 - b_2)$ rose from slightly negative to largely positive from 250°C to 500°C. This suggests that the dry granite may have had the potential for slip instabilities at all temperatures but that the wet granite became essentially stable above 350°C. Given these results, the presence of water on a fault may play an important role in the brittle-ductile transition. While we did not invert for $(a - b)$, we observed increasingly unstable stick-slip with higher temperature, all the way up to the highest temperature we tested, 550°C. This implies that $(a - b)$ is most certainly negative and possibly becoming more negative with higher temperature. This result is unexpected, since it implies a greater tendency for unstable slip at temperatures as high as 550°C and may highlight the control of water on the deep limit of the seismogenic zone. The high temperature stick-slip behavior observed in our experiments will be addressed in a separate study; here we are interested in the origin of an apparent increase in static friction with temperature (Figure 4a). We note that there is no consistent trend in static friction with total slip, except a slight decrease in slope after 360 mm total slip (Figure S10 of the Supplementary Materials). We also do not observe consistent changes in friction depending on the order in which temperature was changed. We visually compared samples with various amounts of total slip, and the gouge volume and particle size distribution looked similar for 80 versus 360 mm of slip. This suggests that friction does not evolve considerably after the initial “run-in” slip. Such behavior helps isolate the effects of temperature on friction.

5. Theoretical Model: Preliminaries

[18] In our experiments, the interaction between the microscopically rough surfaces and gouge particles controls the average value of friction on the slip interface. During “hold” periods, some time-dependent process must result in strengthening of the slip surfaces (or the intervening gouge particles). Here we explore the idea that the logarithmic increase in frictional strength with time results from increases in the real contact area due to creep of highly stressed asperities [*Dieterich and Kilgore*, 1994]. The fractal nature of our model is intended to account for both the microscopically rough geometry of bare surfaces [*Brown and Scholz*, 1985a] as well as the fractal size distribution of gouge particles [*Sammis and Biegel*, 1989]. We use adhesion theory to link true contact area between fractal surfaces to static friction coefficient. The underlying assumption of the model is that increases in real contact area due to viscous flattening of contacts under normal load are the primary cause of the observed logarithmic strengthening of the slip interface during hold time. We seek a model that is also able to reproduce basic characteristics of friction such as Amonton’s laws.

[19] The first Amonton’s law states that the coefficient of friction is independent of total contact area; small and large samples of the same material should have the same friction coefficient. The second law states that shear force at the onset of sliding is proportional to normal force [*Scholz*, 2002]. *Bowden and Tabor* [1950] formulated adhesion theory to explain these empirical relations. The basic tenant of adhesion theory is that when two surfaces come into contact, most of the normal and shear load is supported by a small fraction of the nominal contact area (Figure 5). Asperity contacts, since they are so small, are highly stressed, possibly to the point of yielding, close to the theoretical strength of the order of one tenth of the elastic modulus of the material [*Dieterich and Conrad*, 1984; *Rice et al*., 2001; *Griffith*, 1921]. When a normal force N is applied to the surfaces, the contacts deform and increase in size (in proportion to the normal load) until they are just large enough to support the normal load. A maximum shear force F applied to the surfaces cannot exceed a product of the true contact area of the asperities, A_r, and their intrinsic shear strength, s.

$$F = sA_r \tag{5}$$

[20] The friction coefficient μ is defined as a ratio of F to N, and according to Equation (5) equals

$$\mu = sA_r/N \tag{6}$$

[21] We will use the real area of contact between surfaces, A_r, as a proxy for the coefficient of friction, assuming that the microscopic yield strength s to the first order is independent of temperature. Under this assumption, one can relate second-order changes in the coefficient of friction with time and temperature to evolution of the true contact area,

$$\mu(t, T) = sA_r(t, T)/N \tag{7}$$

[22] In Equation (7), Amonton’s first law (coefficient of friction, μ, is independent of total contact area, A) is satisfied. Under this framework, Amonton’s

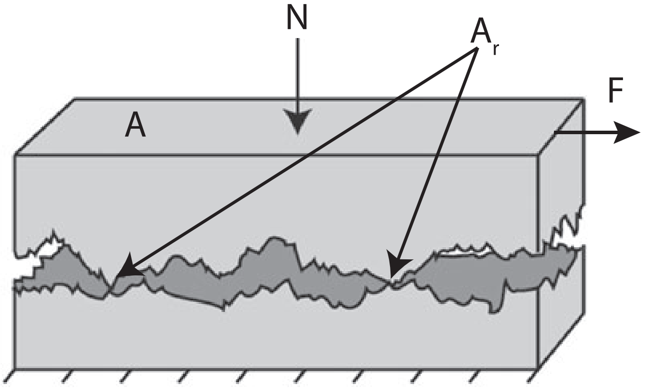

Figure 5. Cartoon of a microscopically rough surface. *N* and *F* are the applied normal and shear forces, respectively. *A* is the total area of contact. A_r, the real contact area, is the sum of many small areas in which the rough surfaces actually touch. A_r is a small fraction of *A*.

second law (*F* is proportional to *N*, or μ is constant) can be explained in one of two ways. In the first explanation, asperities are highly stressed and at the point of plastic yielding, so that normal force, *N*, cannot exceed a product of the real contact area, A_r, and the intrinsic penetration hardness, *p*. From Equation (6), $\mu = s/p$, a constant provided *s* and *p* are material properties, regardless of the contact geometry. If asperities are not at the theoretical strength limit, Amonton's second law cannot be explained by deformation of a single "representative" elastic contact [*Archard*, 1957]. For example, for idealized elastic contacts of spherical shape, A_r is proportional to the normal load as $A_r \propto N^{2/3}$. According to Equation (6), A_r must be linearly proportional to *N* in order to keep μ constant. In the second explanation, true contact area is proportional to the normal load. In the limit of multiple elastic spherical contacts with fractally distributed sizes, A_r becomes directly proportional to *N* [*Archard*, 1957] (Figure S13 of the Supplementary Materials). Both natural faults and cut rock samples are known to have fractal surface geometry with power spectral density decaying as a power law, with power of about −3 to −2, which corresponds to a fractal dimension of 1 to 1.5, over length scales from 100 μm to 0.1 m [*Brown and Scholz*, 1985a]. Some samples exhibited slopes outside this range for certain frequency bands, which yields problems in estimating fractal dimension and scaling up the root mean square (RMS) height to greater wavelengths. The size of our laboratory samples falls within the length scales mentioned above, so we expect the roughness of our samples to be well described by the statistics reported by *Brown and Scholz* [1985a]. *Brown and Scholz* [1985a] suggested that a fractional Brownian surface best describes the observed surface roughness. *Brown and Scholz* [1985b] presented a model in which elastic surfaces with fractal geometry were pressed together. They showed that closure between the surfaces as a function of normal stress successfully predicted closure measured in laboratory experiments on ground glass surfaces which exhibit fractal profiles. Therefore, we adopt this geometry in our numerical models. To reduce the computational burden, we use a 1D realization of the 2D fractional Brownian surface with plane-strain conditions [*Popov*, 2010]. The equivalent contact area can be calculated as

$$A_r = \frac{\pi}{4}\sum_i \left(l_i^2\right) \tag{8}$$

where l_i are the lengths of the "touching" intervals of the 1D interface and a rigid flat surface [*Popov*, 2010]. We also calculated the equivalent contact area as

$$A_r = \sum_i \left(l_i w\right) \tag{9}$$

where *w* is an arbitrary dimension of the slip interface in the direction orthogonal to slip vector. We found that the use of expressions (8) and (9) gives rise to a negligible difference in the ratio of $A_r(t)/A_{ro}$. We have further simplified the model using equivalence between two 1D fractal surfaces and one 1D fractal surface with half the Young's modulus pressed against a rigid flat surface [*Brown and Scholz* , 1985b]. This is justified because the single fractal surface has the same statistical properties, or the same power spectrum, as the difference between two fractal surfaces.

[23] To produce time-dependent evolution of the real contact area under constant normal load, the material must undergo some form of creep. We assume a viscoelastic rheology in which strain rate is some empirical function of deviatoric stress.

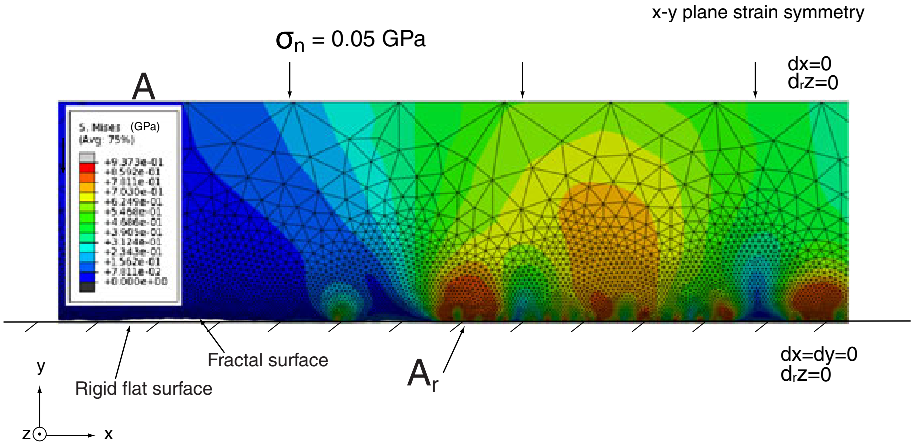

Figure 6. A portion of the finite element model showing model geometry, boundary conditions, loading ($\sigma_n = 0.05$ GPa), and mesh. The distribution of Mises stress is shown, with the color bar in units of gigapascals. Stress concentrations greater than 10 times the applied normal stress can be seen near where the rough surface contacts the flat surface.

$$\dot{\epsilon} = C \exp\left(\frac{-Q}{RT}\right)\sigma_{\text{dev}}^{n} \tag{10}$$

$$\dot{\epsilon} = C \exp\left(\frac{-Q}{RT}\right)\exp(B\sigma_{\text{dev}}) \tag{11}$$

$$\dot{\epsilon} = C \exp\left(\frac{-Q}{RT}\right)[\sinh(B\sigma_{\text{dev}})]^{n} \tag{12}$$

$$\dot{\epsilon} = C \exp\left(\frac{-Q}{RT}\right)\sigma_{\text{dev}}^{n}\exp\left(\frac{\sigma_{\text{dev}}}{\sigma_p}\right) \tag{13}$$

where $\dot{\epsilon}$ is strain rate, C is a premultiplying factor, Q is activation energy, R is the gas constant, T is temperature, σ_{dev} is deviatoric stress, n is the stress power, B is an empirical constant, and σ_p is the Peierls stress. Note that the values of C, B, and n are different in each of the laws and for different materials.

[24] The first creep law (Equation 10) is a power law that, for example, corresponds to migration of imperfections (dislocations) within a crystal lattice, with stress exponent $n \approx 3$ [*Twiss and Moores*, 2007; *Kirby*, 1983]. The second law, exponential creep (Equation 11), is reported to fit steady state creep data on rocks at high stress ($\sigma_{\text{dif}} > 200$ MPa) better than the power law [*Twiss and Moores*, 2007; *Tsenn and Carter*, 1987]. The third law (Equation 12) attempts to fit creep data over a wider range of stresses [*Tsenn and Carter*, 1987; *Post*, 1977]. The fourth law (Equation 13) was proposed as a good fit to high stress olivine creep measurements. Like the exponential and hyperbolic sine laws, the Peierls law is meant to account for the increase in effective stress exponent at high stress [*Renner et al.*, 2002; *Weertman*, 1957; *Evans and Goetze*, 1979]. In addition to the viscous creep law presented in Equation (13), we also specified that there would be a cutoff to viscous behavior at the Peierls stress, σ_p, and that deformation at $\sigma_{\text{dev}} \geq \sigma_p$ would be perfectly plastic.

[25] We used the commercial finite element code Abaqus to perform numerical simulations. First, we generated the fractional Brownian surface with variance of 0.1, Hurst exponent H of 0.6, and total number of points of 5000, using a FORTRAN code from the National Simulation Resource Center for Bioengineering at the University of Washington [*Bassingthwaighte*, 1996]. We used this surface to define a sample geometry and generated a mesh of three-node linear plane-strain triangles. The finest elements of the mesh are defined by the spacing between points on the fractal surface. We also created an analytical rigid flat surface onto which the fractal surface is pressed. We assumed a viscoelastic rheology of the sample, with a viscous creep law presented in Equations (10), (11), and (12). Then we assumed a viscoelastoplastic rheology of the sample, with the viscous creep law presented in Equation (13). We assigned the following boundary conditions: the analytical flat surface is stationary, the top edge of the sample acts as a rigid pin and cannot move in the horizontal (x) direction, and the fractal surface is free of shear stress (free slip boundary condition) and is not allowed to penetrate into or adhere to the rigid foundation (Figure 6). A normal load, σ_n, is applied to the top edge of the sample by ramping linearly up to the desired value within 1 s, then remaining constant for 10^7 s.

[26] One difference between the laboratory experiments and the numerical model is that in the laboratory experiments, the samples were held at both shear and normal stress during hold periods, while the modeled contact was only subjected to normal

stress. To investigate the effect of shear stress on frictional healing in the laboratory, we conducted hold tests at room temperature in which we reduced the shear stress to 0.5 MPa during the hold period. Compared to the hold tests discussed above, hold tests in which shear stress was reduced showed a slight increase in the static coefficient of friction (μ_o was greater by about 3%) and no resolvable change in b. The small difference in results due to reduced-shear stress during hold periods suggests that the model may be describing the healing process well, even without taking shear stress into account. Similar reduced-shear experiments were performed in studies by *Karner and Marone* [2001] and *Nakatani and Mochizuki* [1996]. In hold tests in which the shear stress was reduced to zero, *Karner and Marone* [2001] reported a static coefficient of friction about 8% greater than hold tests performed at shear stress near the sliding value. Similarly, *Nakatani and Mochizuki* [1996] reported that shear unloading during hold periods increased coefficient of friction by 10–20%. This is similar to but of greater magnitude than what we calculate. Both *Karner and Marone* [2001] and *Nakatani and Mochizuki* [1996] reported a decrease in b in reduced-shear hold tests, and *Karner and Marone* [2001] even reported negative b (time-dependent weakening) in tests performed at zero shear stress. This is different from our results, which suggest that b is independent of the shear stress at which the sample is held. According to *Karner and Marone* [2001], deformation of “force chains” within a granular layer can describe the observed variations in μ_s and b with shear stress. We did not include shear loading in the model for two reasons. First, the constitutive relationship for slip at the asperity scale is not well understood but is expected to have a large impact on the predicted shear deformation. Second, our model does not consider breaking of asperities as well as rolling and breaking of gouge particles that presumably play an important role in accommodating shear on natural slip surfaces. We focus on the effects of normal load alone, assuming that the microscopic shear strength is governed by s, while the macroscopic shear strength is governed by the product $sA_r(t)$ (see Equation 7).

6. Numerical Modeling: Results

[27] An acceptable model must be able to reproduce the first-order characteristics of friction such as the Amonton’s laws as well as the second-order characteristics such as the observed rate-, state-, and temperature dependence. First we show that our model obeys Amonoton’s second law in that friction force is proportional to normal force. As described in the previous section, A_r should be proportional to N in order to achieve this [*Greenwood and Williamson*, 1966]. Equivalently, A_r/A is proportional to σ_n, where A is the total area of contact. Here we consider a purely elastic response to an applied normal load. The black curve in Figure (S14) of the Supplementary Materials shows the computed value of A_r/A as a function of σ_n. For a normal stress up to about 0.2 GPa, there is a linear relationship, so the second law is satisfied. At higher stress, the contacts become “saturated” and eventually level off in the limit $A_r/A = 1$. To test whether our model obeys Amonton’s first law (friction is independent of nominal contact area), we ran the same numerical test on fractal surfaces 500, 1000, and 5000 μm long. The results are plotted in Figure (S14) of the Supplementary Materials and show the same slope for $\sigma_n < 0.2$ GPa, indicating that the first law is satisfied as well.

[28] Figure 6 shows the distribution of Mises stress throughout a portion of the model domain. Warm colors represent high stress, and cool colors represent low stress. The places where the fractal surface makes contact with the flat surface are highly stressed, between 0.5 and 0.9 GPa (greater than 10 times the applied normal stress). For applied stresses between 5 and 250 MPa, typical of confining stresses used in most rock friction experiments, the maximum normal stress resolved on the asperities is 2–7 GPa (Figure 7 and Figure S15 of the Supplementary Materials). Adhesion theory holds that local contact stresses are close to the theoretical yield strength of the material, on the order of a few gigapascals [*Rice et al.*, 2001; *Dieterich and Conrad*, 1984]. Our calculations indicate that the maximum contact stress does not scale linearly with the applied normal stress (Figure 7b, light gray line), even in the absence of yielding. Furthermore, the average normal stress supported by the contacts is 0.75–1.7 GPa and is nearly independent of σ_n (Figure 7b, black line). These results suggest that characteristic stresses of the order of a few gigapascals can result from elastic deformation of a fractal surface, and plastic yielding is not required to ensure constant μ [*Greenwood and Williamson*, 1966]. In the viscoelastic model, we ramp σ_n up to 0.05 GPa, higher than the normal stress applied to the samples in the laboratory, 0.015 GPa. This allows for a better sampling of the fractal surface (note how the black line in Figure (S14) of the Supplementary Materials is smoother than the gray lines), and since the stress at the

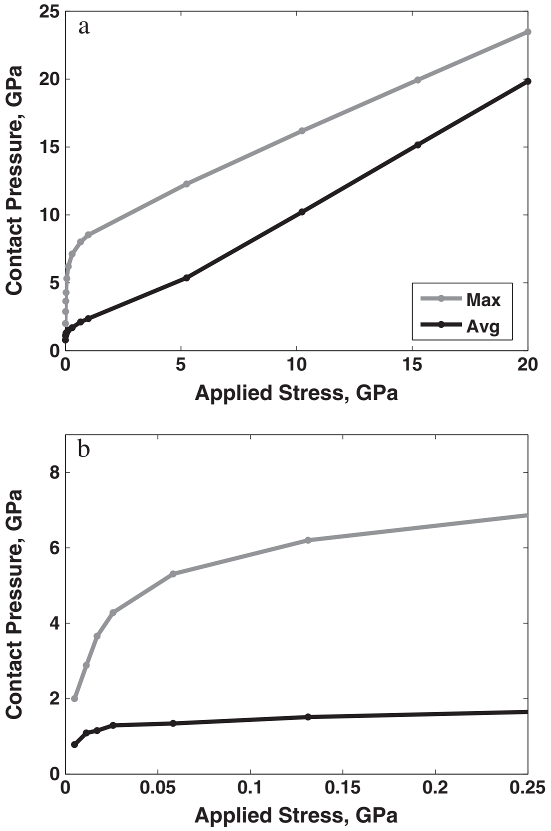

Figure 7. (a) Maximum contact pressure shown in gray and average contact pressure shown in black calculated over the whole fractal surface as a function of applied normal stress. (b) The plot above zoomed in to 0.25 GPa. The average contact pressure changes very little over the applied stress range corresponding to confining pressures applied in most laboratory tests (5–200 MPa). This relationship is a result of the fractal geometry of the contact surfaces and is required by adhesion theory. At very high applied stresses, the fractal surface becomes "saturated," and contact pressure scales linearly with applied stress.

contacts is nearly independent of the applied normal stress within this range of normal stresses, we do not expect the strain rate (and rate of increase in contact area) to be affected by this difference. In the viscoelastic model, the contacts creep and contact area increases, thereby decreasing the local stress concentrations. To model the second-order effects of time and temperature on static friction, we calculate μ_o and b as

$$\mu_o = \frac{sA_{ro}}{\sigma_n A} \tag{14}$$

$$b = \frac{s\Delta A_r}{\sigma_n A \Delta \ln t} \tag{15}$$

and compare to the laboratory data (Figures 10a and 10b). None of the bulk creep laws, when applied to the model, could produce a rate of increase in contact area that matched the rate of increase in static friction observed in our experiments. For example, the power-law rheology pertaining to dislocation creep (Equation 10, n = 3) fails to produce enough deformation in the initial period ($\approx 10^3$ s). This is because the effective viscosity is too high so that the material at first behaves elastically (not flowing and increasing contact area). Furthermore, when the contact area does begin to increase, it does so too quickly (Figure 8, dashed lines). After a parameter search, we found that the power-law rheology is able to explain the laboratory data only if the stress exponent is assumed to be greater than 40. In this case, the model is able to reproduce both short-term effects (aging starts almost immediately) and long-term effects (a relatively constant slope of the aging curves) (Figure 8, solid lines). At this high stress exponent, changing temperature up to 500°C has little effect on the slope of the aging curves, which is consistent with the laboratory data. The best fitting creep laws with parameters deduced bases on trial and error are shown in Figure 9.

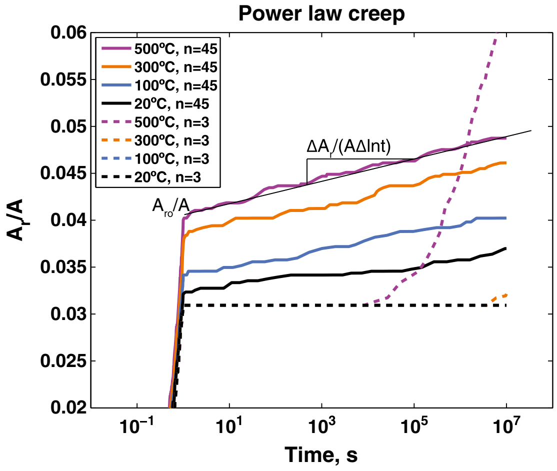

Figure 8. Numerical simulation results for fractional real contact area A_r/A as a function of time. Dashed lines correspond to simulations using a power law pertaining to dislocation creep, with stress power n = 3. Solid lines correspond to simulations using the best fitting power law, with stress power n = 45. Color represents temperature. Note that the dashed lines have a delay during which contact area does not increase, and once contact area does increase, it does so too quickly to match the lab data. The solid lines show real contact area increasing immediately after the normal stress is applied. The higher temperature simulations produce higher values of initial real contact area, similar to the increase in μ_o with temperature observed in the laboratory. The rate of increase in real contact area changes very little as a function of temperature, similar to the insensitivity of slope β observed in the lab.

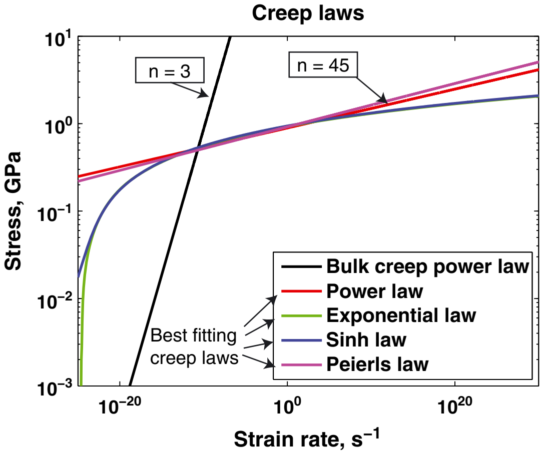

Figure 9. Viscous creep laws used in numerical simulations. For all laws, Q = 105.86 kJ mol^{-1}, R = 8.314 J mol^{-1}K^{-1}, T = 573 K. The bulk creep power law pertaining to dislocation creep is shown in black: $\dot{\epsilon} = C\exp\left(-\frac{Q}{RT}\right)\sigma^n_{\mathrm{dev}}$, where C = 0.7017 GPa^{-3}s^{-1}, n = 3. The best fitting power law is shown in red, where $C = 7.017 \times 10^{11}$ GPa^{-45}s^{-1}, n = 45. The best fitting exponential law is shown in green: $\dot{\epsilon} = C\exp\left(-\frac{Q}{RT}\right)\exp(B\sigma_{\mathrm{dev}})$, where $C = 1 \times 10^{-15}$ s^{-1}, B = 61 GPa^{-1}. The best fitting hyperbolic sine law is shown in blue: $\dot{\epsilon} = C\exp\left(-\frac{Q}{RT}\right)[\sinh(B\sigma_{\mathrm{dev}})]^n$, where $C = 1 \times 10^{-14}$ s^{-1}, B = 20 GPa^{-1}, n = 3. The best fitting Peierls law is shown in magenta: $\dot{\epsilon} = C\exp\left(\frac{-Q}{RT}\right)\sigma^n_{\mathrm{dev}}\exp\left(\frac{\sigma_{\mathrm{dev}}}{\sigma_p}\right)$, where $C = 1 \times 10^{11}$ GPa^{-40}s^{-1}, n = 40, σ_p = 5 GPa.

We also explored a second Peierls creep law: $\dot{\epsilon} = \mathrm{C}\left(\frac{\sigma_{\mathrm{dev}}}{\mu}\right)^1\exp\left(\frac{-\mathrm{Q}}{\mathrm{RT}}\left[1-\left(\frac{\sigma_{\mathrm{dev}}}{\sigma \mathrm{p}}\right)^{\mathrm{m}}\right]^{\mathrm{n}}\right)$ [*Kameyama et al.*, 1999; *Tsenn and Carter*, 1987; *Evans and Goetze*, 1979], with the additional condition that deformation would be perfectly plastic at $\sigma_{\mathrm{dev}} \geq \sigma_p$. It could produce the right slope to fit the experimental data, but the intercept was consistently too low to match the experimental data, so we did not include it with the best fitting laws in Figures 9 and 10. Figure 10 shows a comparison between the lab data and the best fitting numerical results for μ_o and b as a function of temperature. Numerical results using each best fitting creep law from Figure 9 could adequately match the lab data.

7. Discussion

[29] Under the assumption that a fractal contact geometry is a good representation of sheared rock surfaces and that viscous flattening of contacts is responsible for frictional healing, our results indicate that none of the theoretical or empirically derived bulk creep laws are able to explain the observed time and temperature-dependent frictional healing. This result implies several possibilities. First, it is well known that at high stress levels, the power law with n = 3, corresponding to dislocation creep, fails to describe the bulk deformation of rocks [*Twiss and Moores*, 2007]. This "power law breakdown" may be caused by a transition in deformation mechanisms from dislocation creep to dislocation glide around stress of approximately 200 MPa, which may be matched better by a power law with higher n or an exponential law. For

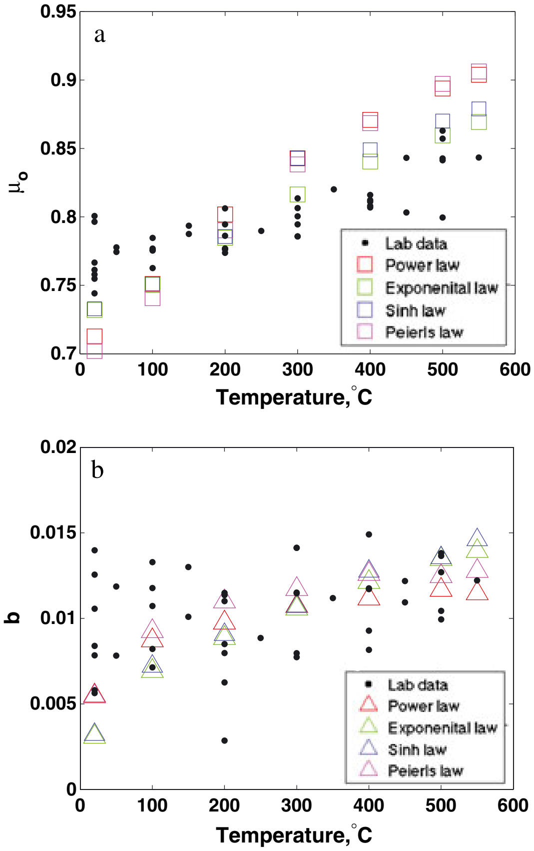

Figure 10. (a) μ_o versus temperature T. Laboratory data are shown in black dots and are calculated using the least squares fit to the data at hold time of 1 s. Results from numerical simulations are shown in squares and are calculated using $\mu_o = \frac{sA_{ro}}{\sigma_n A}$, where s = 1.1 GPa, a material property equal to the shear strength of asperities, A_{ro} is the real contact area reached at 1 s (immediately after the application of normal loading), σ_n = 0.05 GPa, the applied normal loading, and A = 5000 μm^2 is the total area. Color symbols denote the best fitting rheology: power law (red), exponential law (green), hyperbolic sine law (blue), and Peierls law (magenta). (b) Rate-state b parameter versus temperature. Symbol colors are the same as in Figure 10a. Laboratory data are calculated using $b = \frac{\Delta\mu_s}{\Delta \ln t_h}$. Results from numerical simulations are calculated using $b = \frac{s\Delta A_r}{\sigma_n A \Delta \ln t}$.

example, data from high stress creep of clinopyroxenite have been fit by both a power law with $n = 83$ and an exponential law [*Tsenn and Carter*, 1987; *Kirby and Kronenberg*, 1984]. The effective stress exponent of $n \approx 45$ deduced in our study may reflect a similar phenomenon. Second, the bulk rheology reported for macroscopic samples may not be applicable to the deformation of the highly stressed microasperities. Independent measurements of single-crystal hardness have been used to predict a polycrystalline flow law (such as the second Peierls creep law mentioned in section 6) [*Evans and Goetze*, 1979]. Even with modified parameters, this creep law could not match our experimental data. Third, the observed aging effects may be dominated by time-dependent compaction of the gouge layer. In this case, the observed logarithmic strengthening may be due to complex particle interactions that take place in the gouge layer such as sliding and rolling on the inter-grain boundaries [*Frye and Marone*, 2002]. Note that even under conditions of purely uniaxial compression, some fraction of the grain boundaries will be subject to shear stress simply due to the oblique orientation of grain contacts with respect to local principal stresses. Because contact stresses can be locally high, some sliding and rolling between grains may cause a reorganization that leads to a denser gouge packing and greater effective contact area between the surfaces and grains. If this process is more efficient than the bulk viscous deformation of asperities, it could be contributing to the effective high stress exponent needed to match the experimental data. *Karner and Marone* [2001] measured compaction as a function of hold time to compare with measurements of static coefficient of friction. During slide-hold-slide experiments, compaction and static friction increased with the logarithm of hold time, with thicker gouge layers yielding more compaction. While compaction could also result from viscous flattening of asperities, the observed correlation of healing with the thickness of the gouge layer may be evidence for the importance of grain interactions in the recovery of frictional strength. Fourth, the strength of contacting regions, s, may be increasing with time or temperature. It is possible that a combination of $s(t,T)$ (bond "quality") and $A_r(t,T)$ (bond "quantity") contributes to the observed increases in $\mu(t,T)$ [*Frye and Marone*, 2002]. Strengthening of the asperities may be related, e.g., to the development of new bonds across the contacts. *Frye and Marone* [2002] and *Dieterich and Conrad* [1984] studied the effects of humidity on frictional healing. Both studies report that scrupulously dry conditions can severely reduce frictional healing rates. Water-assisted mechanisms may be affecting both the bulk creep of the contacts and the asperity bonds. Hydrolytic weakening may serve to increase contact area or contact "quantity" more quickly. Hydrogen bonding and desorption of water were proposed as possible contact "quality" enhancers, but data collected from the conducted experiments could not distinguish between these two mechanisms [*Frye and Marone*, 2002]. *Dieterich and Kilgore* [1994] directly measured contact area and static coefficient of friction for glass and acrylic. They concluded that growth in contact area is sufficient to explain growth in frictional strength during hold periods. That logarithmic strengthening is observed in various different materials (rock, acrylic, paper, and steel) suggests a common underlying physical mechanism [*Baumberger and Caroli*, 2006]. Thus, results obtained for glass and acrylic may be applicable to a broad range of engineering and geological materials.

8. Conclusions

[30] We ran a series of heated slide-hold-slide laboratory experiments to explore the temperature dependence of frictional healing of Westerly granite. Our results show increases in static coefficient of friction at higher temperature and little dependence of healing rate on temperature. While caution must be used in extrapolating laboratory results to natural faults, our data suggest that neglecting the effect of temperature may lead to underestimation of fault strength under dry conditions by up to 10%. The fault restrengthening rates are only weakly temperature dependent under dry conditions. We performed numerical experiments to test whether temperature-dependent viscous flattening of asperities could account for the frictional restrengthening observed in the lab. We assumed a fractal contact geometry with characteristics similar to those proposed by *Brown and Scholz* [1985a]. We used the evolution of the true contact area as a proxy to time-dependent evolution of the coefficient of friction. We found that rheology corresponding to dislocation creep (power law with stress exponent of 3) fails to match the experimental data. Other creep laws (exponential, hyperbolic sine, and a Peierls creep law) also failed to match the experimental data given the parameters reported in the literature. In order to match the experimental data with a power law, stress exponent of $n > 40$ was required. The other creep laws were also shown to provide a reasonable fit to the lab data given modified model parameters. These results may highlight the

contributions of dislocation glide, grain boundary sliding, gouge compaction, and time-dependent increases in the bond strength in frictional healing. Further work is required to estimate the importance of the proposed mechanisms for fault healing rates

9. Notation

t_h	Hold time, s.
t_o	Hold time = 1 s.
A_r	Real contact area, μm^2.
A_{ro}	Real contact area at t_o, μm^2.
A	Total contact area, μm^2.
μ_s	Static coefficient of friction, dimensionless.
μ_o	Static coefficient of friction at t_o, “intercept,” dimensionless.
β	“Slope” of logarithmic hold time curve, dimensionless.
σ_n	Normal stress, GPa.
σ_s	Shear stress, GPa.
μ_*	Coefficient of friction at reference velocity, V_*, dimensionless.
a	Direct coefficient, dimensionless.
b	Evolution coefficient, dimensionless.
V	Velocity/slip rate between surfaces, μm s^{-1}.
V_*	Reference velocity, μm s^{-1}
θ	State variable, s.
D_c	Critical displacement, μm.
N	Normal force, N.
p	Penetration hardness of asperities, Nm^{-2}.
F	Shear force required to initiate sliding, N.
s	Shear strength of asperities, Nm^{-2}.
l_i	Length of touching intervals between fractal surface and rigid flat surface, μm.
w	Arbitrary dimension of the slip interface orthogonal to the slip vector, μm.
$\dot{\epsilon}$	Strain rate, s^{-1}.
C	Premultiplying factor in steady state creep law, GPa^{-n}s^{-1} for power law and Peierls law, s^{-1} for other laws.
Q	Activation energy, kJ mol^{-1}.
R	Gas constant, kJ mol^{-1} K^{-1}.
T	Temperature, K.
B	Empirical constant, GPa^{-1}.
σ_{dev}	Deviatoric stress, GPa.
n	Stress power, dimensionless.
l, m	Other empirical fitting powers, dimensionless
σ_p	Peierls stress, GPa.
σ_y	Yield stress, GPa.

Acknowledgments

[31] This work was supported by NSF (grant EAR-0838255). This manuscript was improved by insightful reviews by the Associate Editor, Nick Beeler, and Chris Marone.

References

Archard, J. F. (1957), Elastic deformation and the laws of friction, *Proceedings of the Royal Society of London. Series A. Mathematical and Physical Sciences*, *243*(1233), 190–205, doi:10.1098/rspa.1957.0214.

Bassingthwaighte, J. B. (1996), Program to generate fractional Brownian noise using fractional Gaussian processes, *Fortran code Copyright 1995 by National Simulation Resource*, *Univ of WA*., National Simulation Resource Center for Bioengineering, University of Washington, Box 357962, Seattle, WA 98195-7962.

Baumberger, T., and C. Caroli (2006), Solid friction from stick–slip down to pinning and aging, *Advances in Physics*, *55*(3–4), 279–348, doi:10.1080/00018730600732186.

Beeler, N. M., T. E. Tullis, ML Blanpied, and Weeks, J. D. (1996), Frictional behavior of large displacement experimental faults, *J. Geophys. Res.*, *101*(B4), 8697–8715.

Beeler, N. M., T. E. Tullis, and J. D. Weeks (1994), The roles of time and displacement in the evolution effect in rock friction, *Geophys. Res. Lett.*, *21*(18), 1987–1990, doi:10.1029/94GL01599.

Blanpied, M. L. (1995), Frictional slip of granite at hydrothermal conditions, *J. Geophys. Res.*, *100*(B7), 13,045.

Blanpied, M. L., D. A. Lockner, and J. D. Byerlee (1991), Fault stability inferred from granite sliding experiments at hydrothermal conditions, *Geophys. Res. Lett.*, *18*(4), 609.

Blanpied, M. L., C. Marone, D. A. Lockner, J. D. Byerlee, and D. P. King (1998), Quantitative measure of the variation in fault rheology due to fluid–rock interactions, *J. Geophys. Res.*, *103*(B5), 9691.

Bowden, F. P., and D. Tabor (1950), The Friction and Lubrication of Solids, Oxford: Clarendon Press.

Brown, K. M., and Y. Fialko (2012), “Melt welt” mechanism of extreme weakening of gabbro at seismic slip rates, *Nature*, *488*(7413), 638–641.

Brown, S. R., and C. H. Scholz (1985a), Broad bandwidth study of the topography of natural rock surfaces, *J. Geophys. Res.*, *90*(B14), 12,575.

Brown, S. R., and C. H. Scholz (1985b), Closure of random elastic surfaces in contact, *J. Geophys. Res.*, *90*(B7), 5531.

Carter, N., D. A. Anderson, F. D. Hansen, and R. L. Kranz (1981), Creep and creep rupture of granitic rocks, *Geophysical Monograph 24, Mechanical Behavior of Crustal Rocks*, *24*, 61–82.

Chester, F. M. (1995), A rheologic model for wet crust applied to strike-slip faults, *J. Geophys. Res.*, *100*(B7), 13,033–13,044, doi:10.1029/95JB00313.

Collettini, C., A. Niemeijer, C. Viti, and C. Marone (2009), Fault zone fabric and fault weakness, *Nature*, *462*(7275), 907–910.

Di Toro, G., R. Han, T. Hirose, N. De Paola, S. Nielsen, K. Mizoguchi, F. Ferri, M. Cocco, and T. Shimamoto (2011), Fault lubrication during earthquakes, *Nature*, *471*(7339), 494–498.

Dieterich, J. H. (1972), Time-dependent friction in rocks, *J. Geophys. Res.*, *77*(20), 3690–3697, doi:10.1029/JB077i020p03690.

Dieterich, J. H. (1979), Modeling of rock friction 1. Experimental results and constitutive equations, *J. Geophys. Res.*, *84*(B5), 2161–2168, doi:10.1029/JB084iB05p02161.

Dieterich, J. H., and G. Conrad (1984), Effect of humidity on time- and velocity-dependent friction in rocks, *J. Geophys. Res.*, *89*(B6), 4196–4202, doi:10.1029/JB089iB06p04196.

Dieterich, J. H., and B. D. Kilgore (1994), Direct observation of frictional contacts: New insights for state-dependent properties, *Pure and Applied Geophysics*, *143*, 283–302, doi:10.1007/BF00874332.

Evans, B., and C. Goetze (1979), The temperature variation of hardness of olivine and its implication for polycrystalline yield stress, *J. Geophys. Res.*, *84*(B10), 5505–5524.

Fialko, Y. (2004), Temperature fields generated by the elastodynamic propagation of shear cracks in the earth, *J. Geophys. Res.*, *109*(B1), B01,303, doi:10.1029/2003JB002497.

Frye, K. M., and C. Marone (2002), Effect of humidity on granular friction at room temperature, *J. Geophys. Res.*, *107*(B11), 2309, doi:10.1029/2001JB000654.

Goldsby, D. L., A. Rar, G. M. Pharr, and T. E. Tullis (2004), Nanoindentation creep of quartz, with implications for rate- and state-variable friction laws relevant to nanoindentation creep of quartz, with implications for rate- and state-variable friction laws relevant to earthquake mechanics, *Journal of materials research*, *19*(1), 357–365.

Greenwood, J. A., and J. B. P. Williamson (1966), Contact of nominally flat surfaces, *Proceedings of the Royal Society of London. Series A. Mathematical and Physical Sciences*, *295*(1442), 300–319, doi:10.1098/rspa.1966.0242.

Griffith, A. A. (1921), The phenomena of rupture and flow in solids, *Philosophical Transactions of the Royal Society of London. Series A, Containing Papers of a Mathematical or Physical Character*, *221*, 163–198.

Hoskins, E., J. Jaeger, and K. Rosengren (1968), A medium-scale direct friction experiment, *International Journal of Rock Mechanics and Mining Sciences And Geomechanics Abstracts*, *5*(2), 143–152, doi:10.1016/0148-9062(68)90030-2.

Kameyama, M., D. A. Yuen, and S.-I. Karato (1999), Thermal-mechanical effects of low-temperature plasticity (the Peierls mechanism) on the deformation of a viscoelastic shear zone, *Earth and Planetary Science Letters*, *168*(1–2), 159–172, doi:10.1016/S0012-821X(99)00040-0.

Karner, S. L., and C. Marone (2001), Frictional restrengthening in simulated fault gouge: Effect of shear load perturbations, *J. Geophys. Res.*, *106*(B9), 19,319–19,337, doi:Add data for field.

Karner, S. L., C. Marone, and B. Evans (1997), Laboratory study of fault healing and lithification in simulated fault gouge under hydrothermal conditions, *Tectonophysics*, *277*(1–3), 41–55, doi:10.1016/S0040-1951(97)00077-2, earthquake Generation Processes: Environmental Aspects and Physical Modelling.

Kato, N., K. Yamamoto, H. Yamamoto, and T. Hirasawa (1992), Strain-rate effect on frictional strength and the slip nucleation process, *Tectonophysics*, *211*(1–4), 269–282, doi:10.1016/0040-1951(92)90064-D.

Kirby, S. H. (1983), Rheology of the lithosphere, *Rev. Geophys.*, *21*(6), 1458–1487, doi:10.1029/RG021i006p01458.

Kirby, S. H., and A. K. Kronenberg (1984), Deformation of clinopyroxenite: Evidence for a transition in flow mechanisms and semibrittle behavior, *J. Geophys. Res.*, *89*(B5), 3177–3192.

Lockner, D. A., R. Summers, and J. D. Byerlee (1986), Effects of temperature and sliding rate on frictional strength of granite, *Pure and Applied Geophysics*, *124*, 445–469, doi:10.1007/BF00877211.

Marone, C. (1998a), The effect of loading rate on static friction and the rate of fault healing during the earthquake cycle, *Nature*, *391*, 69–72.

Marone, C. (1998b), Laboratory-derived friction laws and their application to seismic faulting, *Annu. Rev. Earth Planet. Sci.*, *26*, 643–696.

Nakatani, M. (2001), Conceptual and physical clarification of rate and state friction: Frictional sliding as a thermally activated rheology, *J. Geophys. Res.*, *106*(B7), 13,347.

Nakatani, M., and H. Mochizuki (1996), Effects of shear stress applied to surfaces in stationary contact on rock friction, *Geophys. Res. Lett.*, *23*(8), 869–872, doi:10.1029/96GL00726.

Nakatani, M., and C. H. Scholz (2006), Intrinsic and apparent short-time limits for fault healing: Theory, observations, and implications for velocity-dependent friction, *J. Geophys. Res.*, *111*(B12), 1–19 doi:10.1029/2005JB004096.

Popov, V. L. (2010), Contact Mechanics and Friction, Springer, Springer Heidelberg Dordrecht London New York.

Post, R. L. (1977), High-temperature creep of Mt. Burnet dunite, *Tectonophysics*, *42*(2–4), 75–110, doi:10.1016/0040-1951(77)90162-7.

Power, W. L., T. E. Tullis, and J. D. Weeks (1988), Roughness and wear during brittle faulting, *J. Geophys. Res.*, *93*(B12), 15,268–15,278.

Renner, J., B. Evans, and G. Siddiqi (2002), Dislocation creep of calcite, *J. Geophys. Res.*, *107*, ECV 6-1–ECV 6-16.

Rice, J. R., N. Lapusta, and K. Ranjith (2001), Rate and state dependent friction and the stability of sliding between elastically deformable solids, *Journal of the Mechanics and Physics of Solids*, *49*(9), 1865–1898, doi:10.1016/S0022-5096(01)00042-4, ¡ce:title¿The JW Hutchinson and JR Rice 60th Anniversary Issue¡/ce:title¿.

Ruina, A. (1983), Slip instability and state variable friction laws, *J. Geophys. Res.*, *88*(B12), 10,359–10,370.

Sammis, C. G., and R. L. Biegel (1989), Fractals, fault-gouge, and friction, *Pure and Applied Geophysics*, *131*, 255–271, doi:10.1007/BF00874490.

Scholz, C. H. (2002), The Mechanics of Earthquakes and Faulting, 2 ed., Cambridge University Press, 40 West 20th Street, New York, NY 10011-4211.

Stesky, R., W. Brace, D. Riley, and P.-Y. Robin (1974), Friction in faulted rock at high temperature and pressure, *Tectonophysics*, *23*(1–2), 177–203, doi:10.1016/0040-1951(74)90119-X.

Stesky, R. M. (1978), Mechanisms of high temperature frictional sliding in Westerly granite, *Canadian Journal of Earth Sciences*, *15*(3), 361–375, doi:10.1139/e78-042.

Tsenn, M. C., and N. L. Carter (1987), Upper limits of power law creep of rocks, *Tectonophysics*, *136*(1-2), 1–26, doi:10.1016/0040-1951(87)90332-5.

Tsutsumi, A., and T. Shimamoto (1997), High velocity frictional properties of gabbro, *Geophys. Res. Lett.*, *24*(6), 699–702, doi:10.1029/97GL00503.

Tullis, J., and R. A. Yund (1977), Experimental deformation of dry Westerly granite, *J. Geophys. Res.*, *82*(36), 5705–5718.

Twiss, R. J., and E. M. Moores (2007), Structural Geology, 2 ed., W. H. Freeman and Company, 41 Madison Avenue, New York, NY 10010.

Weertman, J. (1957), Steady-state creep of crystals, *Journal of Applied Physics*, *28*(10), 1185–1189, doi:10.1063/1.1722604.